Philosophical Magazine

ISSN: 1478-6435 (Print) 1478-6443 (Online) Journal homepage: http://www.tandfonline.com/loi/tphm20

# Atomically resolved precipitates/matrix interfaces in $KTaO_3$ crystals

Y. B. Xu, Y. L. Tang, Y. Liu, X. L. Ma & Y. L. Zhu

**To cite this article:** Y. B. Xu, Y. L. Tang, Y. Liu, X. L. Ma & Y. L. Zhu (2016): Atomically resolved precipitates/matrix interfaces in $KTaO_3$ crystals, Philosophical Magazine, DOI: 10.1080/14786435.2016.1140914

**To link to this article:** http://dx.doi.org/10.1080/14786435.2016.1140914

PHILOSOPHICAL MAGAZINE, 2016
http://dx.doi.org/10.1080/14786435.2016.1140914

Taylor & Francis
Taylor & Francis Group

# Atomically resolved precipitates/matrix interfaces in $KTaO_3$ crystals

Y. B. Xu, Y. L. Tang, Y. Liu, X. L. Ma and Y. L. Zhu

Shenyang National Laboratory for Materials Science, Institute of Metal Research, Chinese Academy of Sciences, Shenyang, China

**ABSTRACT**

$KTaO_3$ is an incipient ferroelectric with its properties influenced by defects and the purity. In this paper, we investigated the microstructures of $KTaO_3$ by X-ray diffraction (XRD) and Cs-corrected scanning transmission electron microscopy (STEM). XRD and electron diffraction indicate that a second phase of $K_6Ta_{10.8}O_{30}$ precipitates from the matrix. Four orientation relationships were identified: $(100)_m$ // $(\bar{3}\,\bar{1}0)_p$, $[001]_m$ // $[0\,0\,1]_p$; $(1\,0\,0)_m$ // $(\bar{1}\,\bar{3}0)_p$, $[001]_m$ // $[0\,0\,1]_p$; $(1\,0\,0)_m$ // $(0\,0\,1)_p$, $[0\,0\,1]_m$ // $[3\,1\,0]_p$ and $(100)_m$ // $(\bar{1}30)_p$, $[0\,0\,1]_m$ // $[3\,1\,0]_p$. High resolution imaging shows that the interfaces between the second phase and $KaTaO_3$ are distinct and coherent. Atomically resolved analysis identified two kinds of novel ordered defects at the interfaces with the termination planes either KO plane of $KTaO_3$ or $TaO_2$ plane of $KTaO_3$.

**ARTICLE HISTORY**
Received 8 September 2015
Accepted 2 January 2016

**KEYWORDS**
High resolution (scanning) transmission electron microscopy; precipitate; interface structures; orientation relationships; $KTaO_3$



## 1. Introduction

$KTaO_3$ crystal is a prototype of $ABO_3$ perovskite oxides exhibiting incipient ferroelectric behaviour and quantum paraelectricity at low temperature in which quantum fluctuation stabilizes the high temperature phase to the lowest temperatures (millikelvins) [1–3]. Recently, a broad range of interests have been excited due to its various unusual properties such as high dielectric permittivity, low dielectric loss and high coordination ability under external fields. In addition, doping and epitaxial strains can be used to modulate polar response of $KTaO_3$, and a ferroelectric $KTaO_3$ could be produced as an environment-friendly ferroelectrics because of its lead-free essence [4,5]. Furthermore, other novel emergent phenomena can also be produced with $KTaO_3$ crystals or related interfaces by doping and epitaxial growth, such as implement superconductivity [6], two-dimensional electron gas etc [7].

It is well known that potential defects and their configurations as well as the purity affect the performance of perovskite films and crystals. Impurities are usually abundant even in nominally pure $KTaO_3$, including magnetic elements Fe and Mn and oxygen vacancies [8–10]. Although many attempts have been made to synthesize high-quality single crystals

**CONTACT** Y. L. Zhu ylzhu@imr.ac.cn

(i.e. with a high homogeneity of chemical and physical properties), there are still some difficulties to acquire a perfect $KTaO_3$ crystal due to the hygroscopicity of the start compounds, microcracks and volatility of potassium oxides upon heating [11,12]. Moreover, during the growth of $KTaO_3$ single crystals, sintering for long time at high temperatures is normally performed in order to eliminate the growth of exaggerated large grains, which in return further deteriorates the potassium loss and favors the formation of $K_6Ta_{10.8}O_{30}$ secondary phase. $K_6Ta_{10.8}O_{30}$ phase is tetragonal with the tungsten bronze structure [11–14]. It is believed that this phase would seriously degrade the quality and block the promising applications of $KTaO_3$ crystals, because many properties such as carrier mobility and dielectric responses depend strongly on the defect density and purities.

Although it is well known that the production of $KTaO_3$ crystals tends to form $K_6Ta_{10.8}O_{30}$ secondary phase, the study of the $K_6Ta_{10.8}O_{30}$ precipitates is relatively insufficient, especially on an atomistic scale. Previously, Axelsson et al. [11,12] synthesized $KTaO_3$ and Mn-doped $KTaO_3$ crystals and evaluated the influence of microstructural features (porosity, structural defects and secondary phases) on the microwave dielectric properties of the ceramic samples. Glinsek et al. [13] prepared $KTaO_3$ by the mechanichemically activated solid-state synthesis. Taishi [14] synthesized $KTaO_3$ by directional solidification. They two detected the presence of second phases in $KTaO_3$ by XRD, which only provides averaged structural information in the reciprocal space in general. From another study, Tchernychova et al. [15] obtained a reliable quantitative composition of $KTaO_3$ by transmission electron microscopy using energy-dispersive X-ray and electron energy-loss spectroscopy. Whereas, the morphology and configurations, possible orientation relationships, atomistic structures and interface structures between $K_6Ta_{10.8}O_{30}$ and $KTaO_3$ are largely neglected. It is believed that these characteristics are of great importance for understanding the formation mechanisms of $K_6Ta_{10.8}O_{30}$ secondary phase and that how they will impact related properties.

Moreover, the atomistic structures and possible defects of/at interfaces between $K_6Ta_{10.8}O_{30}$ and $KTaO_3$ are not only important for understanding the formation of $K_6Ta_{10.8}O_{30}$, but also essential to explore novel functional oxide interfaces, the latter is a fundamental issue in oxide interface fields, which provides vast and unforeseen opportunities for novel designs of electric devices [16–18]. A fundamental understanding of the interface structures at the atomistic scale is considered to be necessary for the further development of crystal properties and the tuning of interface states [19–21]. In this work, $K_6Ta_{10.8}O_{30}$ as a secondary phase in $KTaO_3$ crystals was first investigated by XRD and conventional TEM, and then by Cs-corrected STEM, the latter provides a sub-angstrom level resolution and directly identifies different atom species [22,23]. The morphology, configurations and different types of orientation relationships between $K_6Ta_{10.8}O_{30}$ and $KTaO_3$ were revealed in detail; the atomistic structure of $K_6Ta_{10.8}O_{30}$ and their interface structures were intensively analysed.

## 2. Experimental procedure

Conventional method was used for the preparation of TEM specimens. Briefly, the process includes cutting, grinding, dimpling and finally ion-milling. A Gatan 656 Dimple Grinder was used for dimpling. Ar-ion-milling was performed by using a Gatan 691 Precision Ion Polishing System. A Tecnai G2 F30 transmission electron microscope, equipped with a high-angle-annular-dark-field (HAADF) detector and energy dispersive X-ray spectroscopy systems was used at 300 kV for Z-contrast imaging and composition analysis.

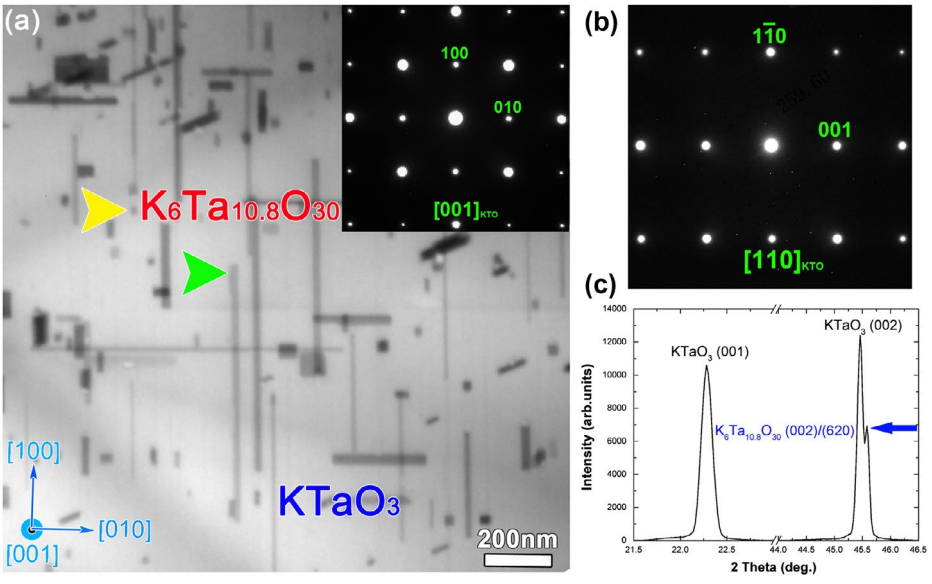


**Figure 1.** (colour online) (a) Bright-field TEM image showing the precipitates within the matrix. Note that the precipitates feature two primary configurations. The inset is a composition diffraction pattern indexed as [1 0 0] zone axis. (b) Composite diffraction pattern of both the matrix and precipitates indexed as [1 1 0] zone axis of $KTaO_3$. (c) XRD patterns showing $K_6Ta_{10.8}O_{30}$ precipitated from $KTaO_3$ crystals.

Atomistic resolution HAADF STEM imaging in this study was performed by using an aberration-corrected scanning transmission electron microscopes (Titan$^3$ $^{TM}$ G2 60-300 microscope fitted with a high-brightness field emission gun and a monochromator, and double Cs correctors from CEOS) operating at 300 kV. Wiener filter is applied in the atomistic resolution HAADF-STEM images [24].

Stereographic projections and simulated electron diffraction patterns were performed with CaRIne Crystallography 3.1 software. Schematic drawings presented in this paper were produced using Vesta [25].

X-ray diffractions were acquired on a Rigaku D/Max-2500PC diffractometer with $\theta$–$2\theta$ scan mode using Cu $K_\alpha$ X-ray irradiation ($\lambda$ = 0.15406 nm). XRD patterns were recorded from 20° to 120° ($2\theta$).

## 3. Results and discussion

### 3.1. General features of $KTaO_3$ crystal structure

Because of the volatile nature of alkali-based compounds, potassium loss is a common problem in the process of sintering $KTaO_3$ crystal, and consequently $K_6Ta_{10.8}O_{30}$ precipitates are generated in the matrix [11–14]. To get information on the size and distribution of $K_6Ta_{10.8}O_{30}$ precipitates, conventional TEM imaging was performed on Tecnai G2 F30 TEM. Figure 1(a) is a bright-field TEM image viewed near the $[0\,0\,1]_m$ direction showing the typical morphology of $K_6Ta_{10.8}O_{30}$ precipitates. It is seen that $K_6Ta_{10.8}O_{30}$ precipitates mainly exhibit two different configurations in $KTaO_3$ crystal, some of them were distributed in the form of stark squares and others showing lamellar appearance, as marked with two arrows,

respectively. The size of stark square shaped precipitates was about 20 nm, while the length of most lamellar precipitates was bigger than 150 nm, with a width around 10 nm. Similar features were observed throughout the sample, and interfaces between those precipitates and $KTaO_3$ crystal were extremely sharp and exhibited a preferential extension along the $\{1\,0\,0\}_m$ faces, suggesting that definite orientation relationships may exist between the second phase and the matrix. The inset of Figure 1(a) is a composite electron diffraction pattern taken from the area including both the matrix and precipitates indexed as [001] of $KTaO_3$. Figure 1(b) is indexed as [1 1 0] zone axis of $KTaO_3$. It is noted that no spot splittings can be clearly identified in the set and in Figure 1(b), implying that the second phase and the matrix may share so similar lattice parameters that they cannot be distinguished from EDPs.

The crystal structure of $KTaO_3$ was probed by using X-ray diffraction. The resulting $\theta - 2\theta$ scans in Figure 1(c) indicate that the crystal apparently crystallizes in a cubic symmetry with a Pm3 m space group, and the lattice parameter of $KTaO_3$ crystal was determined as $a = 3.987 \pm 0.001$ Å, which is consistent with Ref. [26]. In addition, there is a weak diffraction peak at $2\theta = 45.579°$ ($d = 1.989 \pm 0.001$ Å) near $KTaO_3$ {0 0 2} diffraction peak, which demonstrates that there is a second phase in $KTaO_3$ crystal. A careful inspection reveals that this small peak could be referred to {0 0 2} or {6 2 0} peaks of $K_6Ta_{10.8}O_{30}$ precipitates with tetragonal tungsten bronze structure [27]. This indicates that $KTaO_3$ crystal and $K_6Ta_{10.8}O_{30}$ precipitate has a certain orientation relationship of $KTaO_3$ {002} // $K_6Ta_{10.8}O_{30}$ {0 0 2} or $KTaO_3$ {0 0 2} // $K_6Ta_{10.8}O_{30}$ {6 2 0}. No extra peaks can be found, excluding the formation of other precipitates.

### 3.2. Orientation relationships and interface structures between $K_6Ta_{10.8}O_{30}$ and $KTaO_3$

#### 3.2.1. Orientation relationships between $K_6Ta_{10.8}O_{30}$ and $KTaO_3$

The precipitate morphology study implies that $K_6Ta_{10.8}O_{30}$ and $KTaO_3$ probably have certain kinds of orientation relationships. Moreover, the XRD analysis reveal that they do exhibit some orientation relationships like $KTaO_3$ {0 0 2} // $K_6Ta_{10.8}O_{30}$ {0 0 2} or $KTaO_3$ {0 0 2} // $K_6Ta_{10.8}O_{30}$ {6 2 0}. However, due to its finite spatial resolution and information averaging essence, it is difficult to resolve the complete orientation relationships only from XRD.

To determine complete orientation relationships, stereographic projections were drawn to visualize the comparable relations as shown in Figure 2. If we set $[0\,0\,1]_m$ parallel to $[0\,0\,1]_p$ and $[\bar{1}\,0\,0]_m$ parallel to $[3\,1\,0]_p$ in the stereographic projection, as shown in Figure 2(a), then some other parallel relationships can be easily confirmed: $[1\,0\,0]_m$ // $[\bar{3}\,\bar{1}\,0]_p$ and [0 1 0]m // [1 $\bar{3}$0]p. This orientation relationship (short-written as OR1) can also be described by a matrix $M_1$ which transforms a direction in $K_6Ta_{10.8}O_{30}$ to $KTaO_3$ in reciprocal space (Equation (1)), and a matrix $M_1^T$, which converts a plane in $KTaO_3$ to $K_6Ta_{10.8}O_{30}$ in real space (Equation (2)) [28]:

$$\begin{bmatrix} h \\ k \\ l \end{bmatrix}_p = M_1 \begin{bmatrix} h \\ k \\ l \end{bmatrix}_m = \begin{bmatrix} -3 & 1 & 0 \\ -1 & -3 & 0 \\ 0 & 0 & 1 \end{bmatrix} \begin{bmatrix} h \\ k \\ l \end{bmatrix}_m \tag{1}$$

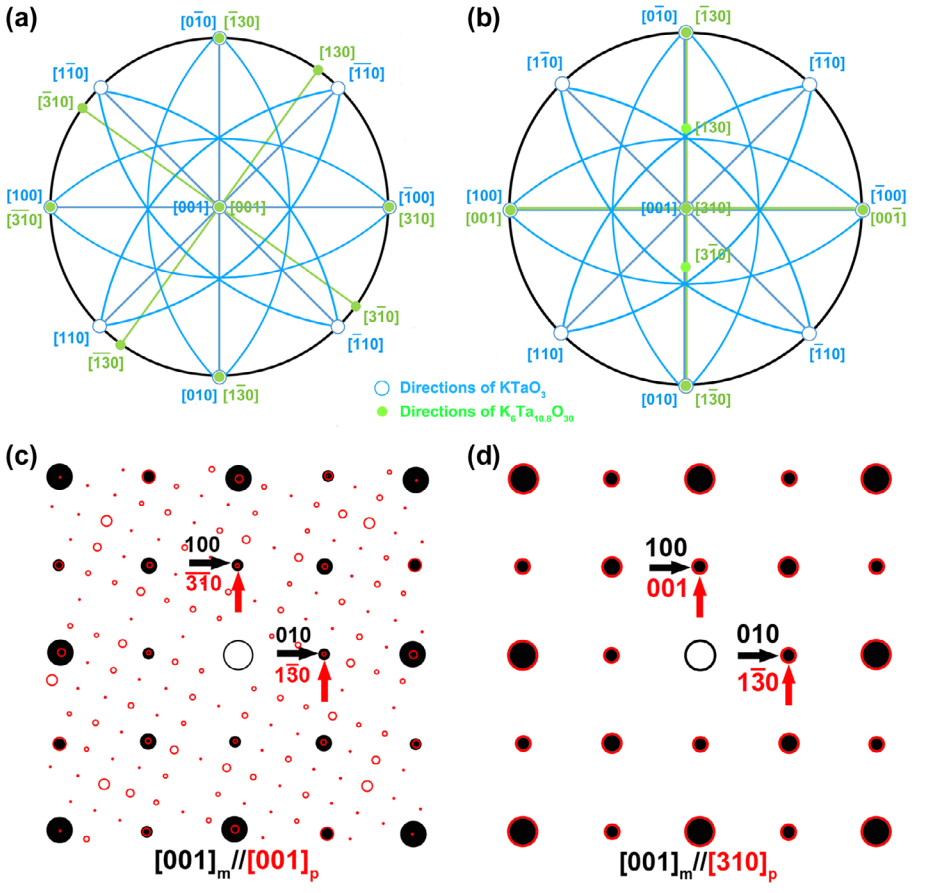


**Figure 2.** (colour online) A stereographic projection showing the orientation relationships between $KTaO_3$ and $K_6Ta_{10.8}O_{30}$. (a) OR1. (b) OR3. Related simulated electron diffraction patterns of (c) OR1 and (d) OR3.

$$\begin{pmatrix} u \\ v \\ w \end{pmatrix}_p = M_1{}^T \begin{pmatrix} u \\ v \\ w \end{pmatrix}_p = \begin{pmatrix} -3 & -1 & 0 \\ -1 & -3 & 0 \\ 0 & 0 & 1 \end{pmatrix} \begin{pmatrix} u \\ v \\ w \end{pmatrix}_p \tag{2}$$

In addition, the stereographic projection of $K_6Ta_{10.8}O_{30}$ in $[0\,0\,1]$ direction is fourfold symmetry, if the stereographic projection of $K_6Ta_{10.8}O_{30}$ rotates 53.13° clockwise along $[0\,0\,1]_p$ in Figure 2(a), another orientation relationships could be obtained: Orientation relationship 2 (short-written as OR2): $[0\,0\,1]_m$ // $[0\,0\,1]_p$, $[1\,0\,0]_m$ // $[\bar{1}\,\bar{3}\,0]_p$ and $[0\,1\,0]_m$ // $3\,\bar{1}\,0_p$.

Based on Figure 1(c), if we set $[0\,0\,1]_m$ parallel to $[3\,1\,0]_p$ and $[\bar{1}0\,0]_m$ parallel to $[0\,0\,\bar{1}]_p$ in the stereographic projection, as shown in Figure 2(b), another orientation relationships could be acquired as well: $[1\,0\,0]_m$ // $[0\,0\,1]_p$, $[0\,1\,0]_m$ // $[1\,\bar{3}\,0]_p$. In the same way, this orientation relationship (short-written as OR3) can also be expressed by a matrix $M_2$ which transforms a direction in $K_6Ta_{10.8}O_{30}$ to $KTaO_3$ in reciprocal space (Equation (3)), and a matrix $M_2^T$, which converts a plane in $KTaO_3$ to $K_6Ta_{10.8}O_{30}$ in real space (Equation (4)):

$$\begin{bmatrix} h \\ k \\ l \end{bmatrix}_{\mathrm{p}} = M_2 \begin{bmatrix} h \\ k \\ l \end{bmatrix}_{\mathrm{m}} = \begin{bmatrix} 0 & 1 & -3 \\ 0 & -3 & 1 \\ 1 & 0 & 0 \end{bmatrix} \begin{bmatrix} h \\ k \\ l \end{bmatrix}_{\mathrm{m}} \tag{3}$$

$$\begin{pmatrix} u \\ v \\ w \end{pmatrix}_{\mathrm{m}} = \begin{pmatrix} u \\ v \\ w \end{pmatrix}_{\mathrm{m}} = {M_2}^T \begin{pmatrix} u \\ v \\ w \end{pmatrix}_{\mathrm{p}} = \begin{pmatrix} 0 & 0 & 1 \\ 1 & -3 & 0 \\ 3 & 1 & 0 \end{pmatrix} \begin{pmatrix} u \\ v \\ w \end{pmatrix}_{\mathrm{p}} \tag{4}$$

Moreover, the stereographic projection of $K_6Ta_{10.8}O_{30}$ in [3 1 0] direction is twofold symmetry, if the stereographic projection of $K_6Ta_{10.8}O_{30}$ rotates 90° clockwise along $[3\,1\,0]_{\mathrm{p}}$ in Figure 2(b), another orientation relationship could be obtained: orientation relationship 4(short-written as OR4): $[0\,0\,1]_{\mathrm{m}}$ // $[3\,1\,0]_{\mathrm{p}}$, $[1\,0\,0]_{\mathrm{m}}$ // $[\bar{1}\,3\,0]_{\mathrm{p}}$ and $[0\,1\,0]_{\mathrm{m}}$ // $[0\,0\,1]_{\mathrm{p}}$.

Because $K_6Ta_{10.8}O_{30}$ has four equivalent ⟨3 1 0⟩, another eight equivalent orientation relationships could be obtained as well. It is understandable that the orientation relationship between the $K_6Ta_{10.8}O_{30}$ and $KTaO_3$ should have 12 forms including 4 independent orientation relationships. Namely, the $K_6Ta_{10.8}O_{30}$ has 12 variants during the precipitation process in $KTaO_3$ matrix. Actually, the different orientation relationships between $K_6Ta_{10.8}O_{30}$ and $KTaO_3$ are originated from the symmetry discrepancies between tetragonal $K_6Ta_{10.8}O_{30}$ and cubic matrix. For validating the veracity of orientation relationships deduced above, diffraction simulation has been carried out as well. Figure 2(c) and (d) shows diffraction simulation results of different zone axes of $K_6Ta_{10.8}O_{30}$ and $KTaO_3$, which are consistent with stereographic projections above. We note that in single-crystal superalloys, the same orientation relationships were experimentally studied between $M_3B_2$ and matrix by TEM [29].

### 3.2.2. Atomistic structures of $K_6Ta_{10.8}O_{30}$ and $K_6Ta_{10.8}O_{30}/KTaO_3$ interface

With the exception of orientation relationships between $K_6Ta_{10.8}O_{30}$ and $KTaO_3$, to understand the atomistic structure of $K_6Ta_{10.8}O_{30}$ is also essential and necessary to know how to tune and control its precipitation behaviour. Moreover, interface structures between $K_6Ta_{10.8}O_{30}$ and $KTaO_3$ are pretty significant for better comprehending their interactions. However, these atomistic details were little known till now. Besides, the atomistic structures of $K_6Ta_{10.8}O_{30}$ and $K_6Ta_{10.8}O_{30}/KTaO_3$ interfaces also provide direct evidences to confirm the orientation relationships deduced above.

Figure 3(a) is an atomically resolved HAADF image showing the $K_6Ta_{10.8}O_{30}/KTaO_3$ interface which was acquired along [001] direction of $KTaO_3$. This interface comes from the square-shaped precipitates in surrounding matrix in Figure 1(a). Under HAADF imaging conditions, the bright spots correspond to the positions of the B-site Ta/O columns, and the weak spots, the A-site K columns. Figure 3(b) is unit cell projections of $KTaO_3$ and $K_6Ta_{10.8}O_{30}$ along [001] directions. At atomistic resolution, the $K_6Ta_{10.8}O_{30}$ / $KTaO_3$ interface is traced as indicated by pink pentagons. It is noted that the interface is not atomically sharp and irregular in shape. The blue squares demonstrate the arrangements of different atom species at the interfaces. It seems that $K_6Ta_{10.8}O_{30}$ precipitate reveals a step-like morphology

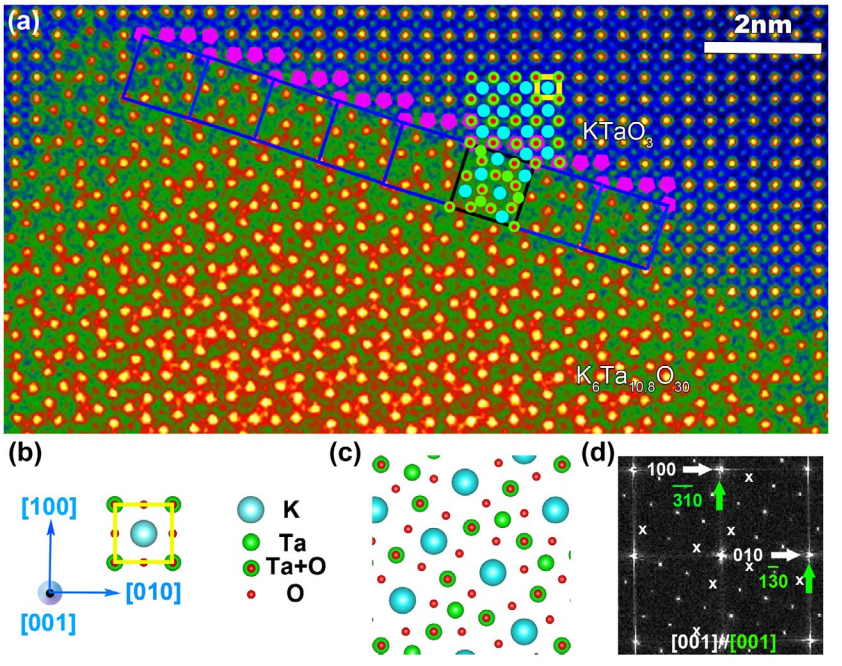


**Figure 3.** (colour online) (a) Atomic-resolution STEM-HAADF image of the $KTaO_3/K_6Ta_{10.8}O_{30}$ interface viewed along the [0 0 1] direction of $KTaO_3$. (b) and (c) are schematic drawing of projections of unit cell along $KTaO_3$ [0 0 1] and $K_6Ta_{10.8}O_{30}$ [0 0 1], respectively. (d) Fourier transform pattern of the STEM-HAADF image showing OR1. The white crosses point to extinct diffracted spots from $K_6Ta_{10.8}O_{30}$.

seen along [001] direction. Figure 3(c) is a projection showing the superimposed atom arrangements at the interface, which is consistent with the atomistic HAADF-STEM image of Figure 3(a). In this direction, $(\bar{3}\,10)$ and $(1\,\bar{3}\,0)$ planes of $K_6Ta_{10.8}O_{30}$ parallel to (1 0 0) and (0 1 0) planes of $KTaO_3$, respectively. The spacing of $(\bar{3}\,10)$ plane of $K_6Ta_{10.8}O_{30}$ is 0.3975 nm, while the spacing of $KTaO_3$ (0 0 1) is 0.3989 nm. Therefore, the interface structure between them is completely coherent, and no misfit dislocations were detected at this interface since the mismatch is negligible. Figure 3(d) was the Fast Fourier Transformation (FFT) pattern of the interface areas in (a), the spots from $KTaO_3$ and $K_6Ta_{10.8}O_{30}$ were indicated with white and green indexes, respectively. This FFT pattern reflects the orientation relationships 1 or 2 as discussed in section 3.2.1, because OR1 and OR2 only have difference in rotation which cannot be distinguished only by one FFT pattern.

Further examination of the lamellar-shaped precipitates revealed that they have extremely sharp interface with $KTaO_3$ matrix. Figure 4(a) is an atomically resolved HAADF-STEM image showing a typical interface structure of the lamellar $K_6Ta_{10.8}O_{30}$ and $KTaO_3$. It is observed that the interface is atomically sharp and perfectly coherent. In order to interpret the structure clearly, we gave projections of unit cell of $KTaO_3$ along [0 0 1] and $K_6Ta_{10.8}O_{30}$ along [3 1 0] directions as shown in Figure 4(b) and (c), respectively. Figure 4(d) is the FFT pattern of the interface areas in (a). White and green indices represent $KTaO_3$ and $K_6Ta_{10.8}O_{30}$, respectively. It is clear that OR3 and OR4 are undistinguishable through the single FFT pattern. In order to solve this problem, we perform intensity profile analysis. An intensity profile shown as an inset in Figure 4(a) indicates the accurate interface position,

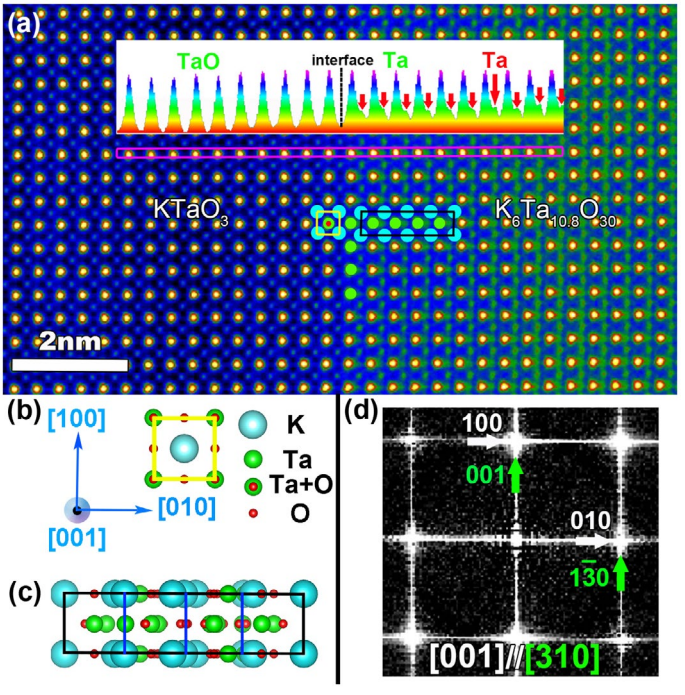


**Figure 4.** (colour online) (a) Atomic-resolution STEM-HAADF image of the $KTaO_3/K_6Ta_{10.8}O_{30}$ interface viewed along the [3 1 0] direction of $K_6Ta_{10.8}O_{30}$. (b) and (c) are schematic drawing of projections of unit cell, along $KTaO_3$ [0 0 1] and $K_6Ta_{10.8}O_{30}$ [3 1 0] directions, respectively. (d) Fourier transform pattern of the STEM-HAADF image showing OR3.

which was ended at KO plane of $KTaO_3$ and $Ta_{10}O_{20}$ plane of $K_6Ta_{10.8}O_{30}$. Small peaks marked by red arrows can be seen in the intensity distribution of $K_6Ta_{10.8}O_{30}$. Based on the [3 1 0] projection of $K_6Ta_{10.8}O_{30}$ (Figure 4(c)), it can be confirmed that the strong and weak peaks come from Ta columns with different densities, as marked by green and red font, respectively. This intensity distribution is consistent with the atomic model shown in Figure 4(a). Combined with the FFT pattern and intensity profile here, it can be deduced that the orientation relationship for Figure 4(a) is OR3. With this orientation relationship, (0 0 1) and (1 $\bar{3}$ 0) planes of $K_6Ta_{10.8}O_{30}$ are parallel to (1 0 0) and (0 1 0) planes of $KTaO_3$, respectively. The spacing of (1 $\bar{3}$ 0) and (0 0 1) planes of $K_6Ta_{10.8}O_{30}$ are 0.3975 and 0.3978 nm, while the spacing of $KTaO_3$ (0 0 1) is 0.3989 nm. Therefore, the interface structure between them is fully coherent, and no misfit dislocations were observed at the interface as well.

In addition, orientation relationship 4 and relevant interface structures were confirmed at an atomic scale as well. High resolution HAADF-STEM image in Figure 5(a) was acquired along the [0 0 1] direction of $KTaO_3$ showing the interface between the lamellar-shaped precipitate and matrix as marked with green arrow in Figure 1. Figure 5(b) and (c) is projections of unit cell of $KTaO_3$ along [0 0 1] and $K_6Ta_{10.8}O_{30}$ [3 1 0] directions. The orientation relationship 3 and 4 can be easily distinguished in atomic-resolution HAADF-STEM images, because there is a 90° rotation between OR3 and OR4 of $K_6Ta_{10.8}O_{30}$ unit cell. Under this orientation relationship, (0 0 1) and ($\bar{1}$ 3 0) planes of $K_6Ta_{10.8}O_{30}$ are parallel to (0 1 0) and (1 0 0) planes of $KTaO_3$, respectively. In the same way, due to the similarity of

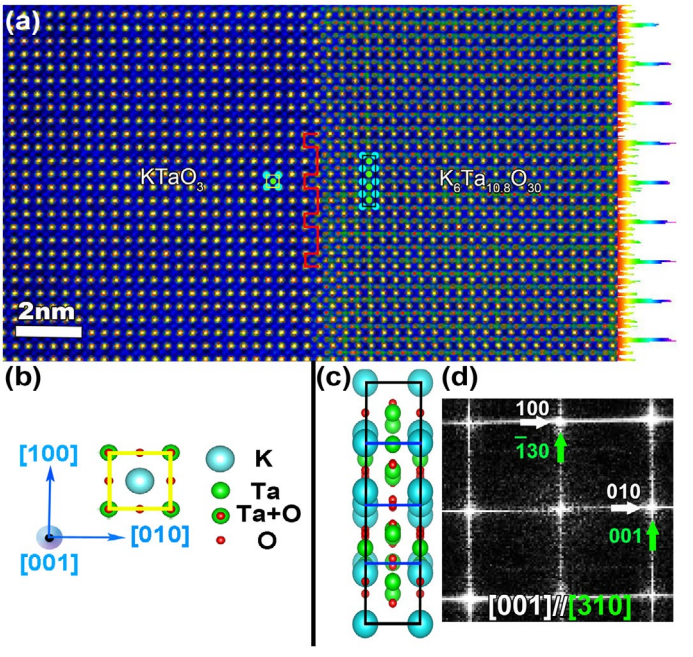


**Figure 5.** (colour online) (a) Atomic-resolution STEM-HAADF image of the $KTaO_3/K_6Ta_{10.8}O_{30}$ interface viewed along the [3 1 0] direction of $K_6Ta_{10.8}O_{30}$, but has different orientation relationship with Figure 4(a). The red lines denote the positions of a novel interfacial defect. (b) and (c) are schematic drawing of projections of unit cell along $KTaO_3$ [0 0 1] and $K_6Ta_{10.8}O_{30}$ [310] directions, respectively. (d) Fourier transform pattern of the STEM-HAADF image showing OR4.

corresponding interplanar spacing, this interface structure is flat. However, different contrast with orientation relationship 3 was observed here, as will be discussed in 3.3. Figure 5(d) was the FFT pattern of the interface areas in (a), white and green indexes represent $KTaO_3$ and $K_6Ta_{10.8}O_{30,}$ respectively.

Besides atomistic structures, electrostatic boundary conditions can be a primary factor dominating the atomistic and electronic structure at oxide interfaces as well [30]. For $KTaO_3$ and $K_6Ta_{10.8}O_{30}$, taking oxygen to have a formal valence of $O^{2-}$, and the K and Ta cations, values of $K^{1+}$ and $Ta^{5+}$, respectively, such that $KTaO_3$ and $K_6Ta_{10.8}O_{30}$ bulk structures remain neutral. It is worth noting that (0 0 1) planes of $KTaO_3$ and (0 0 1) planes of $K_6Ta_{10.8}O_{30}$ are not electrically neutral, which are different from bulk structures. But the charge density of two adjacent planes are the same at the interface in Figure 4(a), and then a polar continuity exists at this interface. Because of no polarity competition at this interface, there was no atomistic reconstruction, and as a result, this interface structure was very sharp and defect free.

### 3.3. Interface defects at $K_6Ta_{10.8}O_{30}/KTaO_3$ interface

Unusual interface structures were found in this study as well. In Figure 5(a), it is noted that the $TaO_2$ layer of $KTaO_3$ connects with the (0 0 1) plane of $K_6Ta_{10.8}O_{30}$ by sharing a $K_xO_y$ layer, and the intensity of columns at this $K_xO_y$ layer exhibits an ordered distribution,

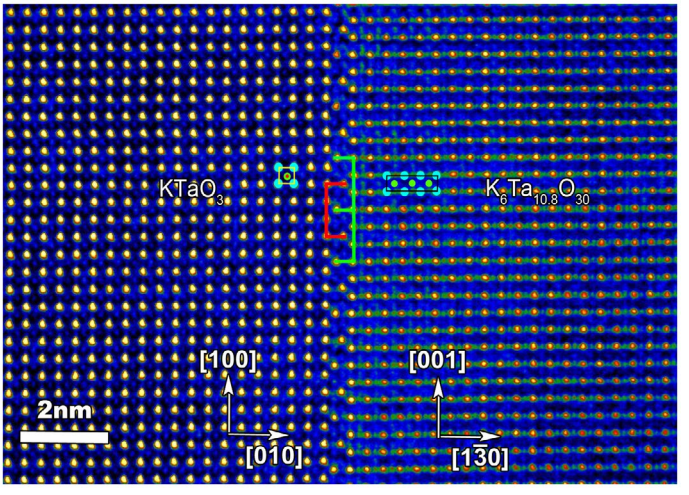


**Figure 6.** (colour online) Atomically resolved STEM-HAADF image showing a novel planar defect, recorded along the [3 1 0] direction of $K_6Ta_{10.8}O_{30}$. The terminated planes are $TaO_2$ plane of $KTaO_3$ and $Ta_{10}O_{20}$ plane of $K_6Ta_{10.8}O_{30,}$ between which have an interfacial bilayer.

which means that there is a bright column between every two KO columns, as the intensity profile indicates (inset). Compared with the intensity of Ta columns in the bulk $K_6Ta_{10.8}O_{30}$, this bright column should enrich Ta element, implying the inhomogeneous chemical distribution at this interface. The ordered defect is marked by a red zigzag line, and it could be clearly shown by the intensity profile along its interface which is shown in Figure 5(a).

In addition, another well-organized defect at the interface can be found in Figure 6, and it was marked by green and red polylines. It can be seen that the continuity of interface structure between $KTaO_3$ and $K_6Ta_{10.8}O_{30}$ is interrupted by the ordered defect. The arrangement of the atoms at the interface plane was different from both the matrix and precipitate. Moreover, a $\langle 110 \rangle$ $a1/2$ relative displacement can be identified between $K_6Ta_{10.8}O_{30}$ and $KTaO_3$, which may be responsible for the formation of this unusual ordered interfacial defect.

Besides the structure displacement, other factors may also contribute to the formation of well-organized defect at the interface, such as for maintaining the local charge neutrality in the area due to possible point defect [31]; interface free-energy minimization process of accommodating the symmetry mismatch between the precipitate and the matrix; partially disordered occupation of Ta in the bulk $K_6Ta_{10.8}O_{30}$ crystal with Ta occupied orderly at the interface. It is expected that theoretical investigations such as ab initio calculations of $KTaO_3/K_6Ta_{10.8}O_{30}$ heterostructures will shed light on understanding why and how those interfacial defects formation is preferential to other options such as misfit dislocations and interfacial bilayer.

## 4. Conclusions

In summary, $K_6Ta_{10.8}O_{30}$ as a second phase formed in $KTaO_3$ crystals and the precipitate/matrix interfaces were investigated by a combination of XRD and transmission electron microscopy analysis. The $KTaO_3$ and $K_6Ta_{10.8}O_{30}$ show clear orientation relationships of $(1\,0\,0)_m // (\bar{3}\,\bar{1}0)_p$, $[001]_m // [0\,0\,1]_p$ (OR1); $(1\,0\,0)_m // (\bar{1}\,\bar{3}0)_p$, $[0\,0\,1]_m // [0\,0\,1]_p$ (OR2); $(1\,0\,0)_m$

// $(0\,0\,1)_p$, $[0\,0\,1]_m$ // $[3\,1\,0]_p$ (OR3) and $(1\,0\,0)_m$ // $(\bar{1}\,3\,0)_p$, $[0\,0\,1]_m$ // $[3\,1\,0]_p$ (OR4). For OR1, the interfaces reveal a step-like morphology seen along [001] direction and with a terminated plane of $TaO_2$. For OR3, the precipitate/matrix interfaces are flat and sharp at the atomistic scale, terminated at KO plane of $KTaO_3$. Two ordered interface defects have been characterized at the interfaces with OR4 and OR3. The former is with interfaces terminated at KO plane of $KTaO_3$, and the chemical distribution at this interface is not homogeneous; the latter, terminated at $TaO_2$ plane of $KTaO_3$ and $Ta_{10}O_{20}$ plane of $K_6Ta_{10.8}O_{30}$. Between these two terminated planes, there is an interfacial layer, at which a $\langle 110 \rangle$ $a1/2$ displacement can be identified.

## Acknowledgements

The authors are grateful to Dr X.B. Hu for fruitful discussions, Mr. B. Wu and Mr. L.X. Yang of this laboratory for their technical support on the Titan platform of the Titan$^{3\,TM}$ G2 60–300 kV aberration-corrected scanning transmission electron microscope.

## Disclosure statement

No potential conflict of interest was reported by the authors.

## Funding

This work was financially supported by the National Natural Science Foundation of China [grant number 51231007], [grant number 51171190]; National Basic Research Program of China [grant number 2014CB921002], [grant number 2009CB623705].

## References

[1] S.H. Wemple, *Some transport properties of oxygen-deficient single-crystal potassium tantalate ($KTaO_3$),* Phys. Rev. 137 (1965), p. A1575–A1582.
[2] L.F. Mattheiss, *Energy bands for $KNiF_3$, $SrTiO_3$, $KMoO_3$, and $KTaO_3$,* Phys. Rev. B 6 (1972), p. 4718–4740.
[3] G.A. Samara, *The relaxational properties of compositionally disordered $ABO_3$ perovskites,* J. Phys.: Condens. Matter. 15 (2003), p. R367–R411.
[4] H. Yokota, Y. Uesu, C. Malibert, and J.M. Kiat, Second-harmonic generation and x-ray diffraction studies of the pretransitional region and polar phase in relaxor K(1−x)LixTaO3, Phys. Rev. B 75 (2007), p. 184113–184118.
[5] M. Tyunina, J. Narkilahti, M. Plekh, R. Oja, R.M. Nieminen, A. Dejneka, and V. Trepakov, *Evidence for strain-induced ferroelectric order in epitaxial thin-film KTaO3,* Phys. Rev. Lett. 104 (2010), p. 227601–227604.
[6] K. Ueno, S. Nakamura, H. Shimotani, H.T. Yuan, N. Kimura, T. Nojima, H. Aoki, Y. Iwasa, and M. Kawasaki, *Discovery of superconductivity in $KTaO_3$ by electrostatic carrier doping,* Nat. Nanotechnol. 6 (2011), p. 408–412.
[7] P.D.C. King, R.H. He, T. Eknapakul, P. Buaphet, S.K. Mo, Y. Kaneko, S. Harashima, Y. Hikita, M.S. Bahramy, C. Bell, Z. Hussain, Y. Tokura, Z.X. Shen, H.Y. Hwang, F. Baumberger, and W. Meevasana, *Subband structure of a two-dimensional electron gas formed at the polar surface of the strong spin-orbit perovskite $KTaO_3$,* Phys. Rev. Lett. 108 (2012), p. 117602–117605.
[8] B. Salce, J.L. Gravil, and L.A. Boatner, *Disorder and thermal transport in undoped $KTaO_3$,* J. Phys.: Condens. Matter. 6 (1994), p. 4077–4092.

[9] V.V. Laguta, M.D. Glinchuk, I.P. Bykov, J. Rosa, L. Jastrabík, R.S. Klein, and G.E. Kugel, *Photochromic centers and impurities in nominally pure $KTaO_3$ and $K_{1-x}Li_xTaO_3$,* Phys. Rev. B 52 (1995), p. 7102–7107.
[10] V.V. Laguta, M.I. Zaritskii, M.D. Glinchuk, and I.P. Bykov, *Symmetry-breaking $Ta^{4+}$ centers in $KTaO_3$,* Phys. Rev. B 58 (1998), p. 156–163.
[11] A.K. Axelsson, Y.Y. Pan, M. Valant, and N.M. Alford, *Synthesis, sintering, and microwave dielectric properties of $KTaO_3$ ceramics,* J. Am. Ceram. Soc. 92 (2009), p. 1773–1778.
[12] A.K. Axelsson, Y.Y. Pan, M. Valant, and N.M. Alford, *Chemistry, processing, and microwave dielectric properties of Mn-substituted KTaO3 ceramics,* J. Am. Ceram. Soc. 93 (2010), p. 800–805.
[13] S. Glinšek, B. Malič, T. Rojac, C. Filipič, B. Budič, and M. Kosec, *$KTaO_3$ ceramics prepared by the mechanochemically activated solid-state synthesis*, J. Am. Ceram. Soc. 94 (2011), p. 1368–1373.
[14] T. Taishi, T. Takenaka, K. Hosokawa, N. Bamba, and K. Hoshikawa, *Growth of potassium tantalate ($KTaO_3$) crystals by directional solidification*, J. Cryst. Growth 380 (2013), p. 39–42.
[15] E. Tchernychova, S. Glinšek, B. Malič, and M. Kosec, *Combined analytical transmission electron microscopy approach to reliable composition evaluation of $KTaO_3$,* J. Am. Ceram. Soc. 94 (2011), p. 1611–1618.
[16] J. Mannhart and D.G. Schlom, *Oxide interfaces-an opportunity for electronics,* Science 327 (2010), p. 1607–1611.
[17] H.Y. Hwang, Y. Iwasa, M. Kawasaki, B. Keimer, N. Nagaosa, and Y. Tokura, *Emergent phenomena at oxide interfaces,* Nat. Mater. 11 (2012), p. 103–113.
[18] M. Fiebig, *Phase engineering in oxides by interfaces,* Philos. Trans. R. Soc. A: Math., Phys. Eng. Sci. 370 (2012), p. 4972–4988.
[19] J. Chakhalian, A.J. Millis, and J. Rondinelli, *Whither the oxide interface,* Nat. Mater. 11 (2012), p. 92–94.
[20] H.Y. Hwang, *Tuning interface states,* Science 313 (2006), p. 1895–1896.
[21] J.W. Reiner, F.J. Walker, and C.H. Ahn, *Atomically engineered oxide interfaces,* Science 323 (2009), p. 1018–1019.
[22] N.D. Browning, M.F. Chisholm, and S.J. Pennycook, *Atomic-resolution chemical analysis using a scannning teansmission electron microscope,* Nature 366 (1993), p. 143–146.
[23] I. MacLaren and Q.M. Ramasse, *Aberration-corrected scanning transmission electron microscopy for atomic-resolution studies of functional oxides,* Int. Mater. Rev. 59 (2014), p. 115–131.
[24] R. Kilaas, *Optimal and near-optimal filters in high-resolution electron microscopy,* J. Microsc. 190 (1998), p. 45–51.
[25] K. Momma and F. Izumi, *VESTA: a three-dimensional visualization system for electronic and structural analysis,* J. Appl. Crystallogr. 41 (2008), p. 653–658.
[26] H.F. McMurdie, M.C. Morris, E.H. Evans, B. Paretzkin, W. Wong-Ng, Y.M. Zhang, and C.R. Hubbard, *Standard X-ray Diffraction Powder Patterns from the JCPDS Research Associateship,* Powder Diffr. 2 (1987), p. 41–52.
[27] A.A. Awadalla and B.M. Gatehouse, *Crystal structures of some nilbium and tantalum oxides. III* $K_6Ta_{10.8}O_{30}$-a partially "filled" tetragonal tungsten bronze-like structure,* J. Solid State Chem. 23 (1978), p. 349–355.
[28] A. Redjaïmia, J.P. Morniroli, P. Donnadieu, and G. Metauer, *Microstructural and analytical study of heavily faulted Frank-Kasper R-phase precipitates in the ferrite of a duplex stainless steel,* J. Mat. Sci. 37 (2002), p. 4079–4091.
[29] N.C. Sheng, X.B. Hu, J.D. Liu, T. Jin, X.F. Sun, and Z.Q. Hu, *$M_3B_2$ and $M_5B_3$ Formation in diffusion-affected zone during transient liquid phase bonding single-crystal superalloys,* Metall. Mater. Trans. A 46 (2015), p. 1670–1677.
[30] N. Nakagawa, H.Y. Hwang, and D.A. Muller, *Why some interfaces cannot be sharp,* Nat. Mater. 5 (2006), p. 204–209.
[31] O. Aktas, S. Crossley, M.A. Carpenter, and E.K.H. Salje, *Polar correlations and defect-induced ferroelectricity in cryogenic $KTaO_3$,* Phys. Rev. B 90 (2014), p. 165309–165310.